nature structural & molecular biology

Structure of myosin-1c tail bound to calmodulin provides insights into calcium-mediated conformational coupling

Qing Lu[1,4], Jianchao Li[1,4], Fei Ye[1,2] & Mingjie Zhang[1–3]

Class I myosins can sense cellular mechanical forces and function as tension-sensitive anchors or transporters. How mechanical load is transduced from the membrane-binding tail to the force-generating head in myosin-1 is unknown. Here we determined the crystal structure of the entire tail of mouse myosin-1c in complex with apocalmodulin, showing that myosin-1c adopts a stable monomer conformation suited for force transduction. The lever-arm helix and the C-terminal extended PH domain of the motor are coupled by a stable post-IQ domain bound to calmodulin in a highly unusual mode. Ca^{2+} binding to calmodulin induces major conformational changes in both IQ motifs and the post-IQ domain and increases flexibility of the myosin-1c tail. Our study provides a structural blueprint for the neck and tail domains of myosin-1 and expands the target binding modes of the master Ca^{2+}-signal regulator calmodulin.

Class I myosins (Myo1s) were the first unconventional myosins identified[1]. They are widely expressed in eukaryotic cells. Humans have eight Myo1 paralogs (Myo1a to Myo1h) out of 24 unconventional myosins, and *Saccharomyces cerevisiae* has two (Myo3p and Myo5p)[2]. In contrast to dimeric myosins (for example, myosin V) that are capable of transporting cargos efficiently along actin filaments[3,4], Myo1s exist as monomers[1,5,6] and can function as force or tension sensors as well as slow transporters[2,7].

Each Myo1 contains, from N terminus to C terminus, a motor domain, a neck region consisting of several calmodulin (CaM)-binding IQ motifs and a tail region. All Myo1s contain a tail homology 1 (TH1) domain featuring an embedded pleckstrin-homology (PH) domain capable of binding to lipid membranes[8–13]. In addition, Myo1s with long tails also contain a TH2 (or GPA) domain and a C-terminal TH3 (or SH3) domain, the latter of which may be responsible for binding to cargos[14]. All Myo1s are capable of bridging actin cytoskeletons with lipid membranes by using their motor heads and tail TH1 domains[2].

Myo1c, a short-tail Myo1 expressed in most tissues (**Fig. 1a**), is involved in numerous physiological processes including sound perception, glucose uptake in various tissues, cell motility and podocyte formation and maintenance[15–19]. Mechanistically, Myo1c is believed to perform its function either by acting as a mechanoforce transducer or sensor, by linking membrane-bound mechanoreceptors with actin filaments underneath (for example, in stereocilia of hair cells)[15], or as a transporter and/or tether, by connecting exocytic vesicles with cortical actin filaments[16,20]. For Myo1c to function as either a force sensor or a tension regulator, its conformation should not be highly flexible, because high flexibility would make mechanical loads applied to the cargo-binding tails difficult to transmit to the motor heads. Indeed, EM structures have revealed that the head, neck and tail of apo-CaM–bound brush-border myosin I (Myo1a) form an elongated and rather rigid structure[21,22], although the low resolution of the EM structures has not provided a detailed atomic picture. High-resolution structural studies of Myo1 have focused on the motor domains[23–25]. No high-resolution structures of the full length or the neck and tail regions of any members of Myo1 are available to date.

CaM is the most versatile Ca^{2+}-signal transducer in all eukaryotes. It contains two similar domains (called N and C lobes), each composed of two Ca^{2+}-binding helix-loop-helix motifs known as EF hands[26]. In the Ca^{2+}-free form, the two helices in each EF hand are nearly antiparallel, forming a closed conformation[27–29]. Upon binding to Ca^{2+}, the two helices become perpendicular, adopting an open conformation[30]. This Ca^{2+}-induced conformational change exposes a hydrophobic pocket in each lobe that facilitates CaM binding to numerous target proteins[31,32]. CaM can also bind to target proteins in its apo form. For example, apo-CaM binds to IQ motifs on myosin heavy chains, thereby stabilizing the helical structure formed by the IQ motifs[33–35]. As with other myosins, Ca^{2+} has vital regulatory roles in Myo1c's functions. For example, Ca^{2+} influxes are believed to trigger the Myo1c-mediated adaptation process in hair cells[15,36], although this view has been challenged recently[37]. Ca^{2+} is also known to be essential for the fusion of Myo1c-tethered vesicles with target membranes[38]. Additionally, Ca^{2+} can also regulate the step sizes and force-sensing

[1]Division of Life Science, Hong Kong University of Science and Technology, Clear Water Bay, Kowloon, Hong Kong, China. [2]Center of Systems Biology and Human Health, School of Science and Institute for Advanced Study, Hong Kong University of Science and Technology, Clear Water Bay, Kowloon, Hong Kong, China. [3]State Key Laboratory of Molecular Neuroscience, Hong Kong University of Science and Technology, Clear Water Bay, Kowloon, Hong Kong, China. [4]These authors contributed equally to this work. Correspondence should be addressed to M.Z. (mzhang@ust.hk).

Received 24 June; accepted 29 October; published online 1 December 2014; doi:10.1038/nsmb.2923

behavior of Myo1s[36,39]. However, the structural basis underlying the CaM-Myo1c interaction and its regulation by Ca^{2+} are unclear.

In this study, we set out to determine the structure of the neck and tail region of Myo1c and to elucidate the Ca^{2+}-induced conformational change of the Myo1c–CaM complex. The findings described in this work provide the first high-resolution structure, to our knowledge, of the neck and tail regions of the ancient single-headed myosin I family. Our study also reveals a previously unrecognized target recognition mode of CaM.

RESULTS

Myo1c is a monomeric motor binding to three CaMs

We characterized the hydrodynamic properties of various segments of the Myo1c tail saturated with apo-CaM by using static light scattering and analytical ultracentrifugation (**Supplementary Fig. 1a–c**). The Myo1c tail spanning from IQ3 to the C-terminal end (amino acids (aa) 742–1028, IQ3-end) in complex with CaM has a measured mass of 47.7 kDa, which matches the theoretical mass of monomeric Myo1c bound to 1 CaM (**Supplementary Fig. 1a,b**). The binding measurement of a shorter fragment lacking the C-terminal PH domain (aa 742–852, IQ3-852) also matches well with a 1:1 stoichiometry of this fragment to CaM (measured mass of 31 kDa versus theoretical mass of 29.8 kDa; **Supplementary Fig. 1c**). Given that IQ1 and IQ2 are canonical apo-CaM–binding motifs, these data indicate that Myo1c should contain only three IQ motifs, as previously reported[40–42]. To further substantiate this conclusion, we measured the molecular masses of CaM-saturated Myo1c tail fragments with their N-terminal boundaries starting either at IQ1 (IQ1-end and IQ1-852) or IQ2 (IQ2-end and IQ2-852) (**Supplementary Fig. 1a–c**). All these Myo1c tails in complex with apo-CaM formed stable monomers in solution. The Myo1c fragments containing all three IQ motifs (IQ1–3 IQ-motif numbering in **Fig. 1a**) each contained three stably bound CaMs, and those containing IQ2 and IQ3 each bound two CaMs. Together, the above biochemical data confirmed that the entire Myo1c tail is a stable monomer, as previously demonstrated for Myo1c[5] and for Myo1b[6].

Overall structure of the Myo1c tail

We obtained good diffraction-quality crystals (up to 3.5-Å resolution) of Myo1c IQ1-end in complex with apo-CaM and solved its structure (**Table 1** and **Supplementary Fig. 2a–d**). The complex adopts an extended architecture with the entire Myo1c tail well structured (**Fig. 1a,b**). The three IQ motifs form a long continuous α-helix. We found that IQ1 and IQ2 each bound to one CaM via the canonical apo-CaM–IQ motif binding mode[34]. The third IQ motif bound to only the C lobe of CaM3; the N lobe unexpectedly bound to a three-helix fragment between IQ3 and the C-terminal extended PH domain (post-IQ domain) (**Fig. 1b**). The final 176-residue stretch of Myo1c forms an extended PH domain, with its N and C termini capped by two α-helices and five β-strands, respectively.

There are extensive interactions between IQ3, the post-IQ domain and the extended PH domain (**Fig. 1b**), thus leading the Myo1c tail–CaM complex to adopt an overall stable conformation (i.e., the entire Myo1c tail forms an integral conformational entity with spatial rigidity). The IQ-motif helix and the post-IQ domain are nearly perpendicular (with an 86° angle between the IQ3 helix and α2), so the entire Myo1c tail complex has an L shape. This near-90° bend between IQ3 and the post-IQ region in our high-resolution structure was also previously observed in the EM images of Myo1a[22], in which the precise region of the bend could not be determined.

IQ motif–CaM interactions

IQ1 and IQ2 of Myo1c bind to apo-CaM via the canonical CaM–IQ motif binding mode (r.m.s. deviation between Myo1c IQ12–apo-CaM_{12} and Myo5a IQ12–apo-CaM_{12} of 1.8 Å) (**Fig. 1c,d**). The C-terminal lobes of CaM1 and CaM2 adopt semiopen conformations in which the CaM hydrophobic pocket anchors the hydrophobic side chain of the IQ motif's isoleucine, and the loop between αF and αG forms hydrogen bonds with glutamine from the IQ motif. The N-terminal lobes of CaM1 and CaM2 remain closed, each interacting weakly with C-terminal hydrophobic residue (Phe719 in IQ1 and Ala742 in IQ2) from the IQ motifs. Of note, the structure of the IQ1–CaM part from our structure and the structure of Myo1c IQ1–CaM[24] can be nicely overlapped with an r.m.s. deviation value of 1.30 Å.

IQ3 interacts with only the C lobe of CaM, which also adopts a semiopen conformation. However, the conformational difference between the C lobe of CaM3 and IQ3 of Myo1c, and the C lobe of CaM and IQ1 of Myo5a is large (r.m.s. deviation of 3.1 Å), thus suggesting that the CaM3-IQ3 interaction deviates from the canonical apo-CaM–IQ interaction. Detailed analysis of the angles between the

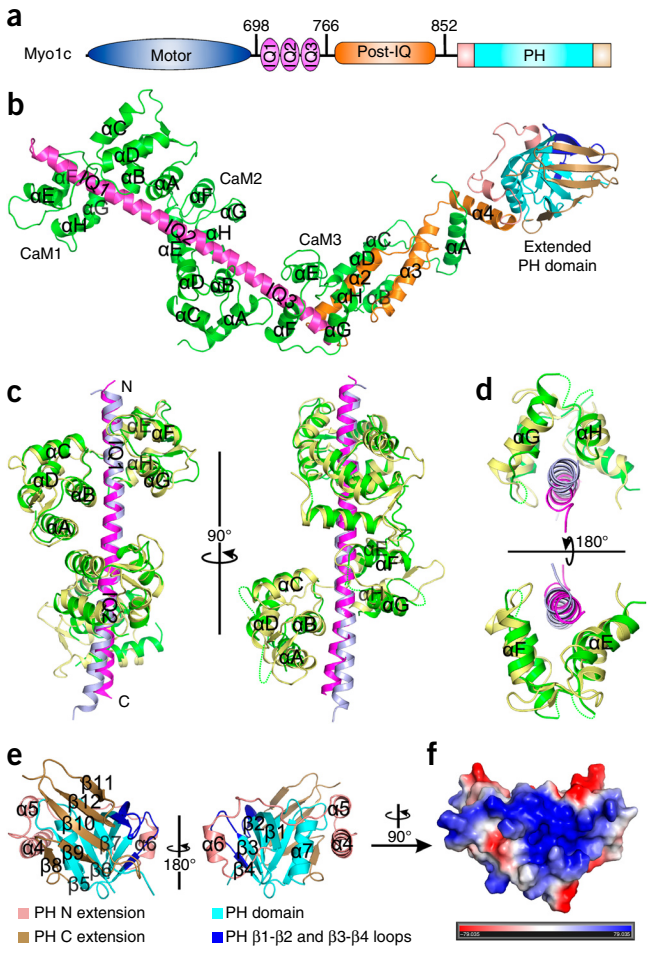

Figure 1 Overall structure of the Myo1c tail bound to apo-CaM. (**a**) Schematic of full-length Myo1c showing domain architecture. (**b**) Ribbon-diagram representations of the overall structure of Myo1c (residue 698 to end, with domains in same colors as in **a**) in complex with three CaM molecules (green). (**c**) Superposition of the Myo1c IQ12–CaM structure with Myo5a IQ12–CaM showing the canonical IQ-CaM binding mode for Myo1c IQ12. (**d**) Superposition of Myo1c IQ3–CaM (C lobe) with Myo5a IQ1–CaM (C lobe). (**e**,**f**) Structure (**e**) and surface electrostatic potential (**f**) of the extended PH domain.

Table 1 Data collection and refinement statistics

	Myo1c neck-tail (native)	Myo1c neck-tail (Au-SAD)
Data collection		
Space group	$P4_32_12$	$P4_32_12$
Cell dimensions		
a, *b*, *c* (Å)	105.4, 105.4, 288.1	105.9, 105.9, 267.9
Resolution (Å)	50–3.5 (3.56–3.50)[a]	50–4.1 (4.17–4.10)
R_{sym}	0.14 (0.88)	0.12 (0.99)
$I / \sigma I$	16.1 (2.4)	33.3 (3.8)
Completeness (%)	99.9 (100)	99.9 (100)
Redundancy	7.2 (7.1)	13.4 (13.7)
Refinement		
Resolution (Å)	50–3.5	
No. reflections	21,359	
R_{work} / R_{free}	0.242 / 0.304	
No. atoms		
Protein	5,555	
Ligand/ion	15	
B factors		
Protein	106.3	
Ligand/ion	141.5	
r.m.s. deviations		
Bond lengths (Å)	0.007	
Bond angles (°)	1.386	

[a]Values in parentheses are for highest-resolution shell. One crystal was used for the native data set, and two crystals were used for the gold-derivative single-wavelength anomalous dispersion (Au-SAD) data set.

two EF-hand pairs showed that the angle between αE and αF is around 110°, a value similar to or slightly larger than that of CaM EF hands in the semiopen conformation[34]. In contrast, the angle between αG and αH of CaM3 is around 130°, resembling that of EF hands adopting a closed conformation, as seen in apo-CaM or the N lobe of apo-CaM bound to canonical IQ motifs[27]. The IQ3 motif contains an arginine (Arg753) instead of glutamine in the signature IQ-dipeptide sequence. Substitution of glutamine with a more bulky arginine may push αG away, causing it to pack with αH in a near-antiparallel manner.

The extended PH domain

The C-terminal 176 residues of the Myo1c tail, known as the TH1 domain, exist in all Myo1s (**Supplementary Fig. 3**). The center of TH1 contains a canonical PH-domain fold formed by a seven-stranded β-barrel and an α-helix (α7) (**Fig. 1e**). A 56-residue fragment (aa 828–883) N terminal to the canonical PH fold forms three α-helices (α4, α5 and α6) and a relatively long loop (the α5-α6 loop), which interact closely with one side of the PH-domain barrel (**Fig. 1e** and **Supplementary Fig. 2d**). The last 52 residues C terminal to the canonical PH fold form five β-strands (β8–β12). The β8 strand is incorporated into the canonical β-barrel of the PH domain by pairing with β5. The strands β9–β12 form another mixed parallel and antiparallel β-sheet, contacting β5–β8 of the PH barrel through hydrophobic interactions. In view of the extensive interactions between the two extension sequences and the canonical PH-domain fold, we believe that the proper folding of the PH domain as well as the entire TH1 domain requires all 176 residues. Thus, we refer to the Myo1c TH1 domain as the extended PH domain. Fitting with our structural data, the frame-shift mutations of Myo1a previously observed in colorectal tumors[43] cause a loss of the last β-strand of the extended PH domain and thus may affect the proper folding of the domain.

The putative lipid-binding pocket is formed primarily by the loops between β1 and β2, and β3 and β4 (shown in blue in **Fig. 1e**) and is located at the end opposite to the motor head. Thus, the lipid-binding pocket of Myo1c is completely accessible to lipid membrane bilayers. Consistently with its role in binding to phosphatidylinositol lipid membranes[11], the extended PH domain of Myo1c contains a prominent positively charged surface centered at the loops connecting β1 and β2, and β3 and β4 (**Fig. 1f**).

Because the amino acid sequences of the TH1 domains among different isoforms of Myo1s are highly conserved (**Supplementary Fig. 3**), we predict that all Myo1s contain extended PH domains capable of binding to lipids[8–10]. It is unclear whether the Myo1c PH domain–extension sequence has additional roles; for example, the extension sequence, alone or together with the PH fold, may be able to bind adaptor proteins or GTPases bound to cargo vesicles.

Unexpected binding between CaM and the post-IQ region

The binding between the post-IQ region of Myo1c and the N lobe of Ca^{2+}-free CaM3 is entirely different from all known CaM-target interactions (**Figs. 1b** and **2a**). In all reported CaM structures, each pair of EF-hand helices assumes one of three conformations: the Ca^{2+}-bound open conformation with the two helices nearly perpendicular, the Ca^{2+}-free closed conformation with the two helices nearly antiparallel or the semiopen conformation in between the open and closed conformations (**Fig. 2d**). In all three conformations, there are direct hydrophobic interactions between the E and F helices. This coupling between E and F helices within each EF hand is also present in all other EF-hand Ca^{2+}-binding proteins with known structures. In sharp contrast, in the complex of the Myo1c post-IQ domain with the N lobe of CaM, the two helices of the first EF hand (αA and αB) of CaM are completely uncoupled (**Fig. 2b**). The αB helix of EF1 associates with the second EF hand (αC and αD), which adopts a closed conformation (**Fig. 2a**), while αA of EF1 is sandwiched between α3 and α4 of the post-IQ domain (**Fig. 2a**,**c**). Myo1c post-IQ α2 and α3 intimately interact with the other three α-helices of CaM, forming a five-helix-bundle structure (**Fig. 2f**). From all CaM structures available in the Protein Data Bank, we calculated the interhelical distances of all EF hands. The interhelical distances of all previously characterized EF hands of CaM are in the range of 5–10 Å (**Fig. 2e**). The interhelical distance of EF1 in Myo1c post-IQ–bound CaM is much larger (~22 Å). Thus, the structure of the Myo1c post-IQ–CaM N-lobe complex reveals a CaM-target binding mode that is radically different from all previous known ones.

The interaction between the Myo1c post-IQ domain and the CaM N lobe can be divided into two hydrophobic-interaction clusters. The first is formed by hydrophobic residues from the α2 and α3 helices on Myo1c and αB, αC and αD of CaM (**Fig. 2f**). The second is formed by residues from the C-terminal half of α3 and Leu836 from α4 of Myo1c and Phe12, Phe16 and Phe19 from the CaM αA helix (**Fig. 2f**). The residues responsible for the interaction between the post-IQ domain and the N lobe of CaM are highly conserved in the class I myosins with short tails (Myo1a, Myo1b, Myo1c, Myo1d, Myo1g and Myo1h; **Supplementary Fig. 3**), thus suggesting that all these Myo1s probably bind to CaM via the mode observed for Myo1c.

The post-IQ region, together with CaM3, also has a critical role in maintaining the rigidity of the Myo1c tail by bridging the IQ motifs and the extended PH domain. There are hydrophobic interactions between IQ3 and α2 of the post-IQ domain (**Fig. 1b** and **Supplementary Fig. 2e**). In addition to binding to αA of CaM, α4 from the post-IQ domain also interacts with α5 and α7 from the extended PH domain via combined hydrophobic and hydrogen-bonding interactions (**Fig. 1b** and **Supplementary Fig. 2f**).

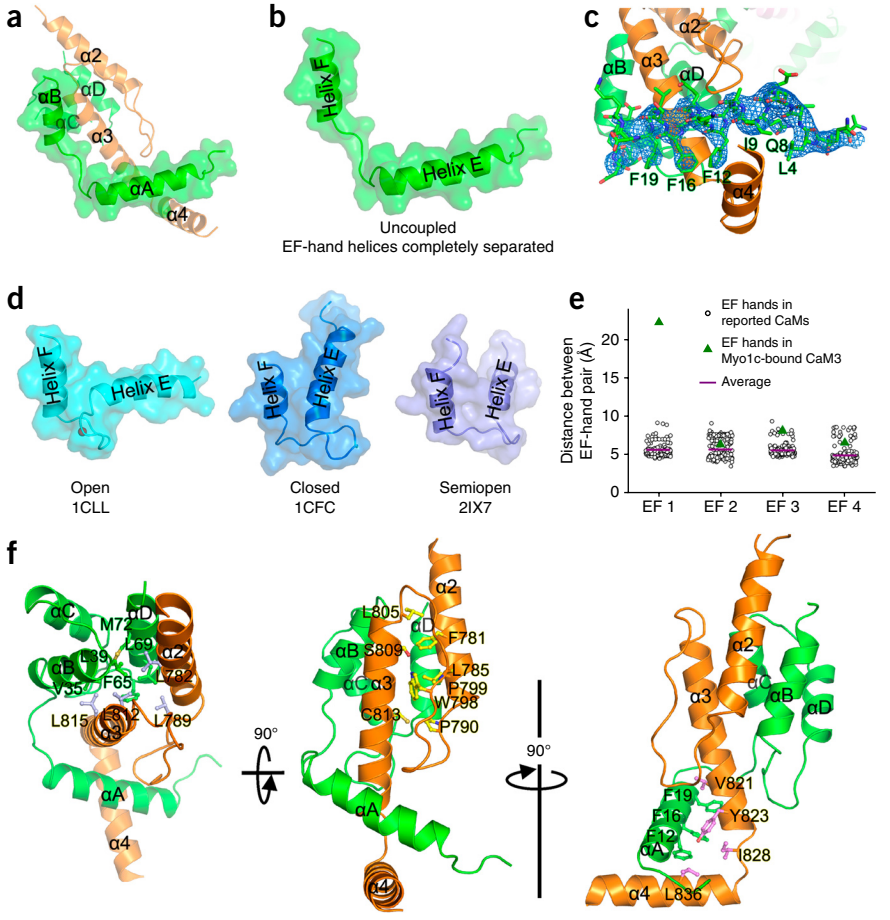

Figure 2 The N lobe of CaM bound to the Myo1c post-IQ domain adopts an uncoupled conformation. (**a**) Binding mode of CaM N lobe (green) and Myo1c post-IQ domain (yellow). (**b**) Structure showing that the αE and αF helices of the first EF hand of the post-IQ–bound CaM are completely separated from each other. (**c**) Omit map of αA of CaM3 bound to the Myo1c post-IQ domain. The $F_o - F_c$ density map was generated by deletion of αA of CaM3 and is contoured at 3.0σ. (**d**) Previously known conformations of Ca^{2+}-binding EF-hand motifs. Left, open conformation with αE and αF nearly perpendicular (represented by Ca^{2+}-bound CaM). Middle, closed conformation with αE and αF nearly antiparallel (represented by apo-CaM). Right, semiopen conformation in between open and closed (represented by the IQ motif–bound CaM). Protein Data Bank accession codes are shown under each model. (**e**) Plot of the interhelical distances of each EF hand found in all CaM structures deposited in the Protein Data Bank (defined as the inter-Cβ distances between interacting hydrophobic-residue pairs in each EF hand: Phe19-Val35 for EF1; Val55-Met71 for EF2; Phe92-Val108 for EF3; and Ala128-Met-144 for EF4). (**f**) The folding core of the Myo1c post-IQ domain and the binding interface between the post-IQ domain and CaM. Left, detailed interactions between the post-IQ domain and αB–αD of CaM. Middle, the folding core of α2, α3 and their connecting loop. Right, hydrophobic interactions between α3 and α4 of the post-IQ domain and αA of CaM.

We performed a series of mutagenesis experiments to test the interaction between the post-IQ region of Myo1c and the N lobe of CaM. Detailed structural analysis of the post-IQ–CaM N-lobe structure revealed that Cys825 from α3 and Phe16 from αA of CaM face each other with their Cβ separated by ~5.7 Å (**Fig. 3a**). In the canonical conformations of CaM EF-hand structures, Phe16 from αA should directly interact with hydrophobic residues from αB (**Fig. 2c**). We reasoned that the substitution of Phe16 of CaM αA with cysteine should promote the formation of a pair of disulfide bonds between Cys16 of CaM and Cys825 of Myo1c if the N lobe of CaM indeed adopts an uncoupled conformation in solution. The ^{15}N-HSQC spectrum showed that Myo1c IQ3-852 in complex with F16C CaM is properly folded and adopts a similar overall structure to that of Myo1c IQ3-852 in complex with wild-type CaM (**Supplementary Fig. 4a**). By simply exposing the freshly purified, reduced form of the Myo1c IQ3-852–F16C CaM complex to ambient air oxygen at 4 °C overnight, we obtained a near-complete covalent Myo1c–CaM complex with 1:1 stoichiometry. Addition of DTT to this oxidized sample reversed the formation of the covalent complex (**Fig. 3b**).

We further investigated the interaction between the post-IQ domain of Myo1c and the N lobe of CaM by using a loss-of-function approach in heterologous cells. In this assay, we took advantage of the structure showing that the IQ3-852 fragment is the minimal and sufficient region of Myo1c to interact with CaM3 (**Figs. 1b** and **2f**). In COS7 cells, overexpression of wild-type GFP–Myo1c IQ3-852 alone (**Fig. 3c**) restricted fluorescence signals to the nucleus, probably owing to the abundant solvent-exposed, positively charged residues in the IQ3 and post-IQ regions of Myo1c. When RFP-tagged CaM was coexpressed, wild-type GFP–Myo1c IQ3-852 translocated to the cytoplasm to colocalize with CaM (**Fig. 3c**). We then substituted Leu782 from α2 and Leu815 from α3 of the Myo1c post-IQ domain with glutamate, either individually or together, to test the interaction between the Myo1c post-IQ domain and the CaM N lobe on CaM-induced cytoplasmic localization of Myo1c IQ3-852. On the basis of the structure shown in **Figure 2f**, any one of these mutations should disrupt the interaction between Myo1c IQ3-852 and CaM. Consistently with our predictions, L782E, L815E and L782E L815E Myo1c IQ3-852 all showed restricted nuclear localization (**Fig. 3c**,**d**) with coexpressed CaM diffused throughout the cells, thus further validating the interaction between the Myo1c post-IQ domain and CaM shown in **Figure 2**.

Finally, we demonstrated, using NMR spectroscopy, that Myo1c IQ3 binds to only the C lobe of CaM. During titration of the IQ3 peptide into ^{15}N-labeled apo-CaM, only the backbone peaks from the C lobe underwent chemical-shift changes (**Supplementary Fig. 4b**, with shift assignment from ref. 27).

CaM–post-IQ interaction is required for Myo1c's function

In polarized Madin-Darby canine kidney (MDCK) cells, knockdown of Myo1c has been shown to reduce the stability of E-cadherin at lateral cell-cell adhesion sites[44], possibly by weakening the connections between cortical actin cytoskeletons and lateral plasma membranes. In agreement with the data in a recent study[44], we found that wild-type full-length Myo1c colocalizes well with E-cadherin at the lateral membranes and adherens junctions, but not with ZO-1, in polarized MDCK cells (**Fig. 4a**). In contrast, the GFP-tagged L782E L815E Myo1c did not associate with E-cadherin and becomes diffused in the cytoplasm instead (**Fig. 4a**). Additionally,

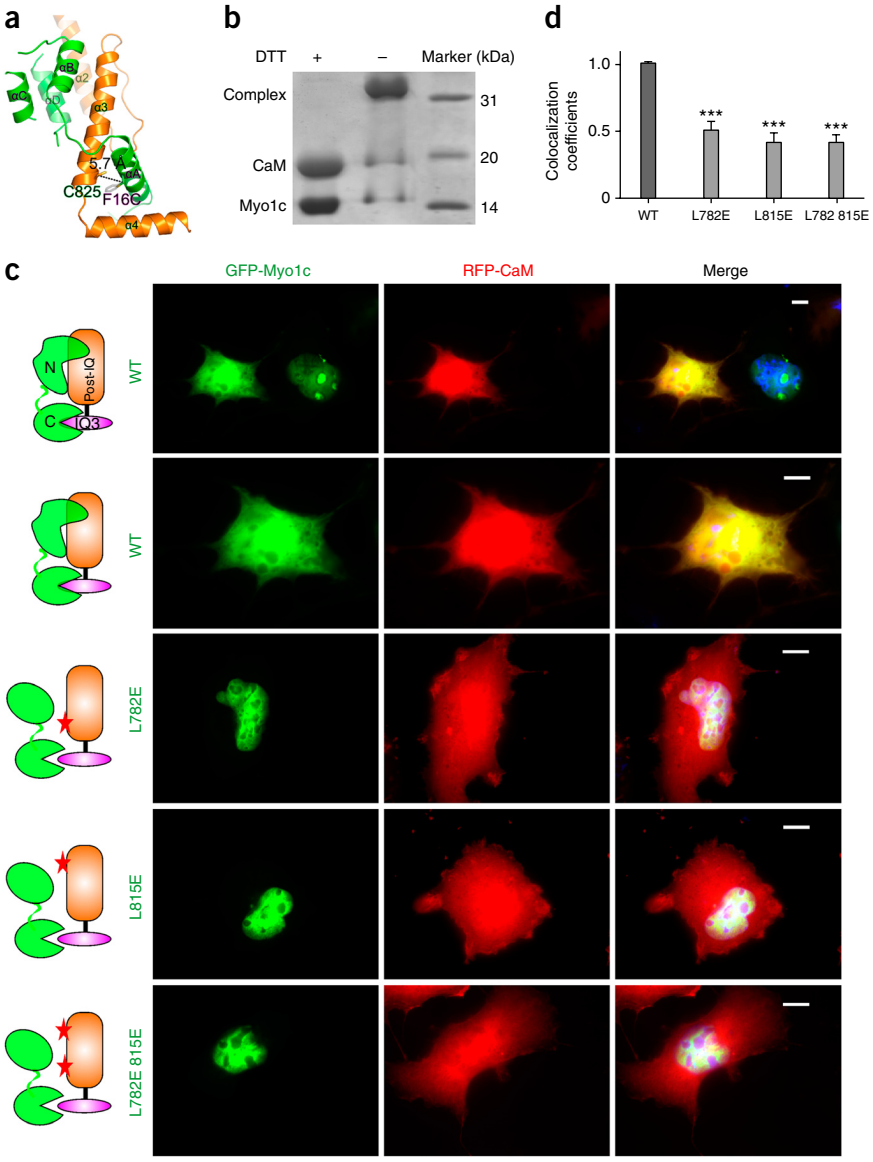

Figure 3 Validation of the interaction between post-IQ Myo1c and CaM. (**a**) Ribbon diagram of the interaction between the Myo1c post-IQ domain (yellow) and CaM N lobe (green), showing that Cβ of Cys825 from Myo1c is 5.7 Å from the Cβ of Phe16 from CaM. (**b**) SDS-PAGE showing disulfide-bond formation between Myo1c IQ3-852 and F16C CaM upon air oxidation (–) and reversal of the disulfide bond upon treatment of the oxidized complex with 10 mM DTT (+). (**c**) Representative images of overexpressed GFP–Myo1c IQ3-852 and its mutants (green) with or without coexpressed RFP-CaM (red) in COS-7 cells ($n = 15$ randomly picked cells). Nuclei are stained with 4′, 6-diamidino-2-phenylindole (DAPI) in blue. Scale bars, 10 μm; top row is zoomed out to show two cells in one image. WT, wild type. (**d**) Quantification of colocalization of GFP–Myo1c IQ3-852 and RFP-CaM in COS-7 cells. Mander's colocalization coefficient for single channel is measured. Error bars, s.d. ($n = 15$ randomly picked cells). ***$P < 0.001$ by two-tailed Student's t test.

overexpression of GFP-tagged L782E L815E Myo1c caused E-cadherin to be partially mistargeted to the basal membranes in polarized MDCK cells, a defect similar to that caused by knockdown of endogenous Myo1c[44]. The above data suggest that the new binding mode between CaM and the post-IQ region plays a critical part in Myo1c's function in maintaining adherens junctions in polarized MDCK cells.

Calcium-induced structural changes

It is generally agreed that binding of Ca^{2+} will result in dissociation of one CaM from Myo1c[40,42,45]. However, the exact regions of Myo1c to which the remaining two Ca^{2+}-bound CaMs bind are not known. Additionally, the post-IQ region has not often been included in previous analyses of the interaction between Ca^{2+}-CaM and Myo1c[41,42,45] and thus could lead to an incomplete picture of the interaction.

We performed a series of detailed biochemical and biophysical analyses of the interactions between Ca^{2+}-CaM and the Myo1c tail. Fast protein liquid chromatography (FPLC) coupled with light-scattering studies showed that the addition of 1 mM Ca^{2+} to the Myo1c IQ1-end–CaM complex led to an ~20-kDa decrease in molecular mass (**Fig. 5a**) consistent with the loss of one CaM from the complex. Unexpectedly, the addition of 1 mM Ca^{2+} to a mixture of Myo1c IQ3-852 with excess apo-CaM produced a Myo1c IQ3-852–Ca^{2+}-CaM complex peak with a molecular mass ~20 kDa larger than the Myo1c IQ3-852–apo-CaM complex peak (**Fig. 5a**), thus indicating that the IQ3 and post-IQ region of Myo1c can bind to two Ca^{2+}-CaMs. Together, the above biochemical results reveal that, at saturated Ca^{2+} concentrations, CaM1 and CaM2 dissociate from IQ1 and IQ2, respectively; the IQ3 post-IQ region binds to an additional CaM, and thus the entire Myo1c tail retains two Ca^{2+}-CaMs. Our isothermal titration calorimetry (ITC)-based assay (**Fig. 5d**) also confirmed the previous finding that Myo1c IQ2 has only a very weak affinity (K_d ~21 μM) for Ca^{2+}-CaM[42,45]. It is possible that the Ca^{2+}-induced dissociation from IQ1 may not occur in the full-length Myo1c, considering that IQ1-bound CaM has been shown to directly couple with the motor domain[24,25].

We next tested whether the tail region of Myo1c becomes flexible upon Ca^{2+} binding to CaM. We used partial proteolytic digestions to probe the conformational flexibilities of the IQ1-end and IQ2-end of Myo1c with and without Ca^{2+} (**Supplementary Fig. 5a–c**). The results invariably demonstrated that the addition of Ca^{2+} accelerates both trypsin and thrombin digestion rates of the Myo1c tail, thus indicating that the conformation of the motor tail is more flexible upon Ca^{2+} binding to CaM. This conclusion is also supported by a CD spectroscopy–based study of Myo1c IQ2-852 (**Supplementary Fig. 5d**).

We then investigated the interaction between the IQ3 post-IQ region of Myo1c and Ca^{2+}-CaM. We found that removal of the residues corresponding to α4 of Myo1c (aa 829–852) did not alter its interaction with Ca^{2+}-CaM, thus indicating that α4 of the post-IQ region is not involved in Ca^{2+}-CaM binding (**Supplementary Fig. 6**). Next, we used synthetic peptides corresponding to IQ3 (aa 744–764), α2 (aa 769–788) and α3 (aa 804–827) to study their interactions

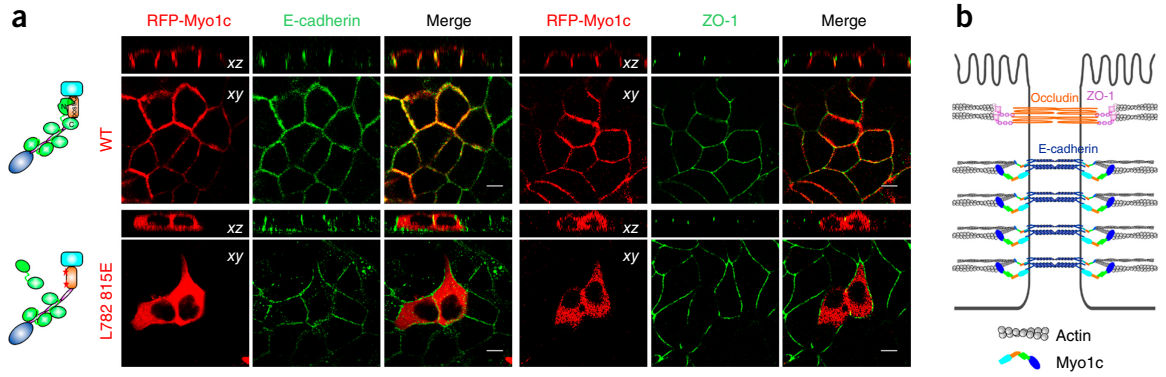

Figure 4 The new interaction between CaM and the Myo1c post-IQ domain is required for proper function of Myo1c. (**a**) Representative images of overexpressed full-length RFP-Myo1c (red) in polarized MDCK cells (n = 10 cells randomly picked from three independent experiments). Anti–E-cadherin antibody and ZO-1 staining (green) are used to mark lateral membranes and tight junctions, respectively. Scale bars, 5 μm. An *xz* section is shown at the top of each column, and a single optical *xy* section of the corresponding image is shown below the *xz* section. (**b**) Schematic diagram showing that Myo1c is required for maintaining adherens junctions in polarized MDCK cells.

with Ca^{2+}-CaM. ITC-based experiments showed that the IQ3 peptide bound to Ca^{2+}-CaM with very strong affinity (K_d ~60 nM), and the α3 peptide bound to Ca^{2+}-CaM with a K_d of ~1.3 μM (**Fig. 5b**). The α2 helix had no detectable binding to Ca^{2+}-CaM (**Fig. 5d**). NMR-based titration experiments showed that the IQ3 and α3 peptides each bind to both lobes of Ca^{2+}-CaM with 1:1 stoichiometry, because the residues from both lobes of Ca^{2+}-CaM underwent peptide binding–induced chemical-shift changes (**Fig. 5c**). We also studied the interactions between the IQ3, α2 and α3 peptides and apo-CaM by using ITC. Neither α2 nor α3 showed detectable binding to apo-CaM (**Fig. 5d**), in agreement with our structural analysis that the CaM–post-IQ interaction requires simultaneous interactions between the entire post-IQ region of Myo1c and the N lobe of CaM (**Fig. 2f**). Although occupying only the C lobe of CaM, the IQ3 peptide bound to apo-CaM with a moderate affinity (K_d ~3.1 μM, **Fig. 5d**).

In summary, when the concentration of Ca^{2+} rises, one CaM remains bound to IQ3 with high affinity, and CaM's binding to IQ1 and IQ2 weakens. The post-IQ region must undergo considerable conformational changes in order to free up α3 for

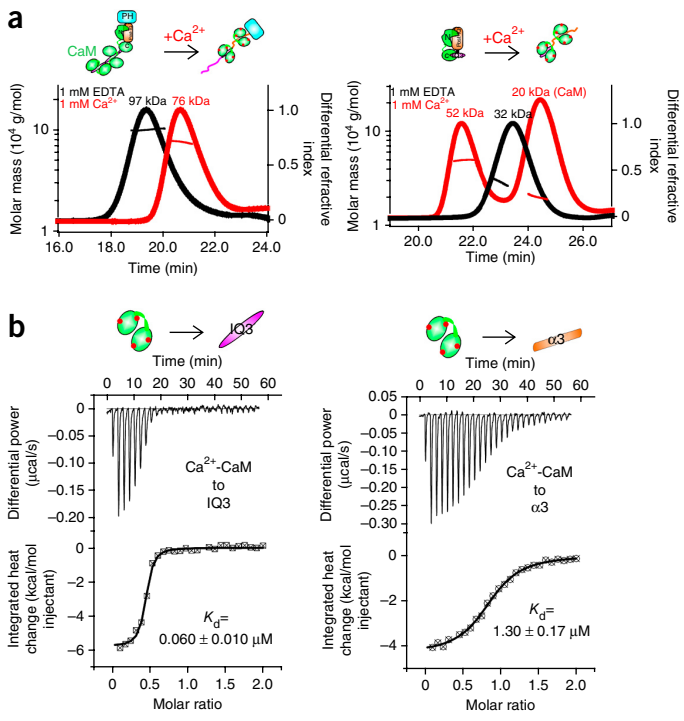

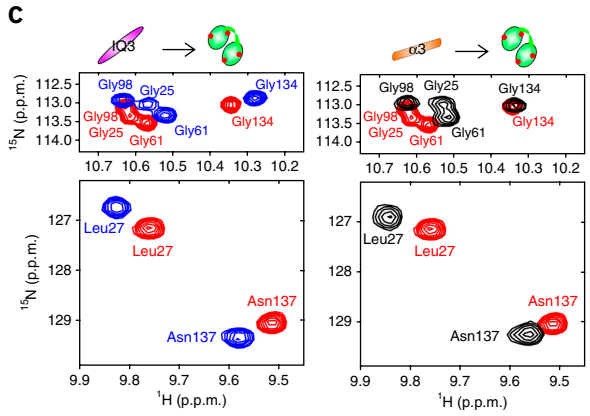

d

	K_d (μM) Ca^{2+}	K_d (μM) EDTA
IQ2	20.7 ± 4.4	0.49 ± 0.03
IQ3	0.06 ± 0.01	3.14 ± 0.86
α2	Undetectable	Undetectable
α3	1.30 ± 0.17	Undetectable

Figure 5 Calcium-induced structural changes of the Myo1c tail. (**a**) FPLC coupled with static light-scattering analysis, showing the binding of Myo1c to apo-CaM (black) and Ca^{2+}-CaM (red). Myo1c IQ1-end (left) and IQ3-852 (right) are both saturated with an excess amount of CaM. (**b**) ITC titration curves showing the binding affinities of the IQ3 peptide (left) and the α3 peptide (right) with Ca^{2+}-CaM. (**c**) ^{15}N-HSQC spectra showing the titration of the IQ3 peptide (left) or the α3 peptide (right) to ^{15}N-labeled Ca^{2+}-CaM. For clarity, only the two end points are shown: before addition of each peptide to CaM (red) and after the saturation of CaM with each peptide (IQ3 peptide (blue, left) or α3 peptide (black, right)). (**d**) ITC titration–derived affinities of CaM with various Myo1c fragments.

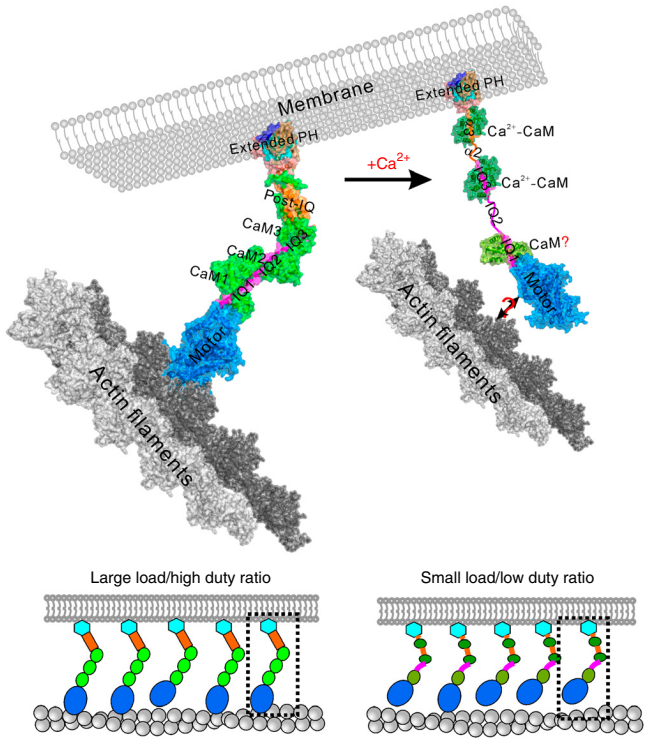

Figure 6 Schematic model for Myo1c-mediated tethering between actin filaments and Myo1c-bound membranes. The model of the full-length Myo1c structure was obtained by superposition of the IQ1–CaM1 of our tail structure and that of the Myo1b structure solved recently[25]. Tensions or loads generated by the binding between the extended PH domain and lipid membranes can be transduced to the motor head bound to the actin filament when Myo1c is bound to apo-CaM. Binding of Ca^{2+} to CaM leads to dissociation of CaM from IQ2, and possibly from IQ1, and to major conformational changes in the post-IQ region of Myo1c, converting Myo1c from the rigid conformation to a more flexible conformation. Myo1c in the flexible conformation would have diminished loads, and this would further promote the dissociation of the motor head from the actin filaments, owing to its low duty ratio under small load.

binding to both lobes of Ca^{2+}-CaM. Because neither α2 nor α4 is involved in binding to Ca^{2+}-CaM, it is most likely that these two regions will also become flexible when Myo1c is bound to Ca^{2+}-CaM (**Fig. 6**).

DISCUSSION

The most salient feature of the Myo1c structure determined in this work is that the entire tail adopts a rigid monomeric structure. From the recently reported crystal structures of the motor domains of Myo1b and Myo1c[24,25], we built a structural model of the full-length Myo1c. According to this modeled structure, full-length Myo1c should also adopt a stable monomeric conformation in which its actin-binding motor domain and lipid membrane–binding extended PH domain point in opposite directions (**Fig. 6**). The post-IQ region of Myo1c, together with CaM, plays a pivotal part in coupling the N-terminal IQ motifs and C-terminal extended PH domain. As such, the overall topology and structural rigidity are suited for Myo1c to transduce tension forces between the motor head and the membrane-binding tail. Because the post-IQ region is highly conserved in several Myo1s with short tails (Myo1a, Myo1b and Myo1h in particular; **Supplementary Fig. 3**), it is likely that these Myo1s also adopt conformations similar to that of Myo1c. The extended, rigid structures of the class I family myosins are also supported by the previous EM studies of Myo1a[22] and Myo1c[5].

Another important structural feature is that the tail of Myo1c undergoes a Ca^{2+}-dependent flexibility change, which is mediated via its light-chain CaM. When Ca^{2+} concentration increases, the dissociation of CaM from IQ motifs can affect the stiffness of the IQ-motif helix. The conformational rearrangement of the post-IQ region induced by Ca^{2+}-CaM binding further increases the tail flexibility of Myo1c. The Ca^{2+}-induced tail-flexibility change has also been indicated in an EM study of Myo1a[46]. The loss of tail rigidity might cause a dissipation of tension between the motor head and the cargo-binding tail of Myo1c and probably those of other Myo1s as well (**Fig. 6**). It has been reported that when load is released the duty ratio and power output of Myo1c also decrease[7,47], although Myo1c is less sensitive to the applied load when compared to Myo1b[7,47,48]. The decrease of the duty ratio can in return promote detachment of the motor from actin filaments and eventual total uncoupling between Myo1c-bound cargo vesicles and actin filaments (**Fig. 6**). When cells return to their resting state, the drop in the cellular Ca^{2+} concentration allows Myo1c to return to its rigid, apo-CaM–bound conformation. Therefore, Myo1c and Myo1b[39], and probably Myo1a and Myo1h as well, may undergo Ca^{2+}-dependent cycling between rigid and flexible conformers. In a manner reminiscent of the rapid Ca^{2+}-induced activation of Ca^{2+}-channels by resident CaMs[49], the speedy recovery of Myo1c to its rigid conformational state upon Ca^{2+}-concentration drop may be facilitated by the remaining Ca^{2+}-CaMs bound to the Myo1c tail.

As the most important Ca^{2+}-signal transducer, CaM is known to interact with hundreds of target proteins in both its apo and Ca^{2+}-bound states. The basic structural unit of CaM is the EF-hand helix-loop-helix motif, which is capable of responding to cellular Ca^{2+}-concentration changes. EF hands also occur in numerous other Ca^{2+}-binding proteins with diverse cellular roles[50]. The interaction between the Myo1c post-IQ domain and the N lobe of CaM reveals an unexpected interaction mode between CaM and its targets. In this interaction, the E helix of the first EF hand is completely separated from its F helix and from the second EF hand (**Fig. 2**). Instead of recognizing a few key hydrophobic residues observed in CaM adopting canonical conformations, this uncoupled conformation of the CaM N lobe binds to an array of hydrophobic residues from three different α-helices of Myo1c (**Fig. 2f**), forming a specific CaM–post-IQ complex that is critical for Myo1c's functions (**Figs. 3** and **4**). Importantly, the interaction between CaM with an uncoupled conformation and Myo1c post-IQ is also Ca^{2+} dependent (**Fig. 5**). Therefore, the interaction between CaM and the Myo1c post-IQ domain observed in this study represents a new paradigm of target recognition and Ca^{2+}-dependent regulation for CaM. Our finding opens the possibility that CaM, and potentially numerous other EF-hand Ca^{2+}-binding proteins, may recognize additional target proteins by adopting uncoupled EF-hand conformations.

In summary, the structure of the Myo1c tail presented here, together with recently published motor-domain structures, provides a framework for understanding the cellular functions of the Myo1 family motors. The Myo1c-CaM interaction also expands the range of target recognition modes of CaM and probably of other EF-hand Ca^{2+}-binding proteins.

METHODS

Methods and any associated references are available in the online version of the paper.

Accession codes. Coordinates and structure factors for the Myo1c tail in complex with CaM have been deposited in the Protein Data Bank under accession code 4R8G.

Note: Any Supplementary Information and Source Data files are available in the online version of the paper.

ACKNOWLEDGMENTS

We thank the BL17U station at the Shanghai Synchrotron Radiation Facility for X-ray beam time; Y. Zhang for technical help; and members of the Zhang laboratory for comments on the manuscript. This work was supported by grants from the Research Grant Council of Hong Kong (663811, 663812, 664113, HKUST6/CRF/10, SEG_HKUST06, T13-607/12R and AoE/M09/12 to M.Z.) and the National Key Basic Research Program of China (2014CB910204 to M.Z.). We thank C. Petit (Institut Pasteur) for the full-length *Myo1c*.

AUTHOR CONTRIBUTIONS

Q.L., J.L. and M.Z. designed experiments and analyzed data. Q.L., J.L. and F.Y. performed experiments. Q.L., J.L. and M.Z. wrote the manuscript. M.Z. coordinated the research.

COMPETING FINANCIAL INTERESTS

The authors declare no competing financial interests.

1. Pollard, T.D. & Korn, E.D. *Acanthamoeba* myosin: I. Isolation from *Acanthamoeba castellanii* of an enzyme similar to muscle myosin. *J. Biol. Chem.* **248**, 4682–4690 (1973).
2. McConnell, R.E. & Tyska, M.J. Leveraging the membrane: cytoskeleton interface with myosin-1. *Trends Cell Biol.* **20**, 418–426 (2010).
3. Hartman, M.A., Finan, D., Sivaramakrishnan, S. & Spudich, J.A. Principles of unconventional myosin function and targeting. *Annu. Rev. Cell Dev. Biol.* **27**, 133–155 (2011).
4. Hammer, J.A. III & Sellers, J.R. Walking to work: roles for class V myosins as cargo transporters. *Nat. Rev. Mol. Cell Biol.* **13**, 13–26 (2012).
5. Batters, C. *et al.* Myo1c is designed for the adaptation response in the inner ear. *EMBO J.* **23**, 1433–1440 (2004).
6. Stafford, W.F., Walker, M.L., Trinick, J.A. & Coluccio, L.M. Mammalian class I myosin, Myo1b, is monomeric and cross-links actin filaments as determined by hydrodynamic studies and electron microscopy. *Biophys. J.* **88**, 384–391 (2005).
7. Greenberg, M.J. & Ostap, E.M. Regulation and control of myosin-I by the motor and light chain-binding domains. *Trends Cell Biol.* **23**, 81–89 (2013).
8. Adams, R.J. & Pollard, T.D. Binding of myosin-I to membrane lipids. *Nature* **340**, 565–568 (1989).
9. Miyata, H., Bowers, B. & Korn, E.D. Plasma-membrane-association of *Acanthamoeba* myosin-I. *J. Cell Biol.* **109**, 1519–1528 (1989).
10. Hayden, S.M., Wolenski, J.S. & Mooseker, M.S. Binding of brush border myosin I to phospholipid vesicles. *J. Cell Biol.* **111**, 443–451 (1990).
11. Hokanson, D.E., Laakso, J.M., Lin, T., Sept, D. & Ostap, E.M. Myo1c binds phosphoinositides through a putative pleckstrin homology domain. *Mol. Biol. Cell* **17**, 4856–4865 (2006).
12. Komaba, S. & Coluccio, L.M. Localization of myosin 1b to actin protrusions requires phosphoinositide binding. *J. Biol. Chem.* **285**, 27686–27693 (2010).
13. Patino-Lopez, G. *et al.* Myosin 1G is an abundant class I myosin in lymphocytes whose localization at the plasma membrane depends on its ancient divergent pleckstrin homology (PH) domain (Myo1PH). *J. Biol. Chem.* **285**, 8675–8686 (2010).
14. Krendel, M., Osterweil, E.K. & Mooseker, M.S. Myosin 1E interacts with synaptojanin-1 and dynamin and is involved in endocytosis. *FEBS Lett.* **581**, 644–650 (2007).
15. Holt, J.R. *et al.* A chemical-genetic strategy implicates myosin-1c in adaptation by hair cells. *Cell* **108**, 371–381 (2002).
16. Bose, A. *et al.* Glucose transporter recycling in response to insulin is facilitated by myosin Myo1c. *Nature* **420**, 821–824 (2002).
17. Tiwari, A., Jung, J.J., Inamdar, S.M., Nihalani, D. & Choudhury, A. The myosin motor Myo1c is required for VEGFR2 delivery to the cell surface and for angiogenic signaling. *Am. J. Physiol. Heart Circ. Physiol.* **304**, H687–H696 (2013).
18. Arif, E. *et al.* Motor protein Myo1c is a podocyte protein that facilitates the transport of slit diaphragm protein Neph1 to the podocyte membrane. *Mol. Cell. Biol.* **31**, 2134–2150 (2011).
19. Fan, Y., Eswarappa, S.M., Hitomi, M. & Fox, P.L. Myo1c facilitates G-actin transport to the leading edge of migrating endothelial cells. *J. Cell Biol.* **198**, 47–55 (2012).
20. Boguslavsky, S. *et al.* Myo1c binding to submembrane actin mediates insulin-induced tethering of GLUT4 vesicles. *Mol. Biol. Cell* **23**, 4065–4078 (2012).
21. Jontes, J.D., Wilson-Kubalek, E.M. & Milligan, R.A. A 32° tail swing in brush border myosin I on ADP release. *Nature* **378**, 751–753 (1995).
22. Jontes, J.D. & Milligan, R.A. Brush border myosin-I structure and ADP-dependent conformational changes revealed by cryoelectron microscopy and image analysis. *J. Cell Biol.* **139**, 683–693 (1997).
23. Kollmar, M., Durrwang, U., Kliche, W., Manstein, D.J. & Kull, F.J. Crystal structure of the motor domain of a class-I myosin. *EMBO J.* **21**, 2517–2525 (2002).
24. Münnich, S., Taft, M.H. & Manstein, D.J. Crystal structure of human myosin 1c—the motor in GLUT4 exocytosis: implications for Ca^{2+} regulation and 14-3-3 binding. *J. Mol. Biol.* **426**, 2070–2081 (2014).
25. Shuman, H. *et al.* A vertebrate myosin-I structure reveals unique insights into myosin mechanochemical tuning. *Proc. Natl. Acad. Sci. USA* **111**, 2116–2121 (2014).
26. Kretsinger, R.H. & Nockolds, C.E. Carp muscle calcium-binding protein: II. Structure determination and general description. *J. Biol. Chem.* **248**, 3313–3326 (1973).
27. Zhang, M., Tanaka, T. & Ikura, M. Calcium-induced conformational transition revealed by the solution structure of apo calmodulin. *Nat. Struct. Biol.* **2**, 758–767 (1995).
28. Kuboniwa, H. *et al.* Solution structure of calcium-free calmodulin. *Nat. Struct. Biol.* **2**, 768–776 (1995).
29. Finn, B.E. *et al.* Calcium-induced structural-changes and domain autonomy in calmodulin. *Nat. Struct. Biol.* **2**, 777–783 (1995).
30. Babu, Y.S. *et al.* Three-dimensional structure of calmodulin. *Nature* **315**, 37–40 (1985).
31. Ikura, M. *et al.* Solution structure of a calmodulin-target peptide complex by multidimensional NMR. *Science* **256**, 632–638 (1992).
32. Hoeflich, K.P. & Ikura, M. Calmodulin in action: diversity in target recognition and activation mechanisms. *Cell* **108**, 739–742 (2002).
33. Terrak, M., Wu, G.M., Stafford, W.F., Lu, R.C. & Dominguez, R. Two distinct myosin light chain structures are induced by specific variations within the bound IQ motifs: functional implications. *EMBO J.* **22**, 362–371 (2003).
34. Houdusse, A. *et al.* Crystal structure of apo-calmodulin bound to the first two IQ motifs of myosin V reveals essential recognition features. *Proc. Natl. Acad. Sci. USA* **103**, 19326–19331 (2006).
35. Terrak, M., Rebowski, G., Lu, R.C., Grabarek, Z. & Dominguez, R. Structure of the light chain-binding domain of myosin V. *Proc. Natl. Acad. Sci. USA* **102**, 12718–12723 (2005).
36. Adamek, N., Coluccio, L.M. & Geeves, M.A. Calcium sensitivity of the cross-bridge cycle of Myo1c, the adaptation motor in the inner ear. *Proc. Natl. Acad. Sci. USA* **105**, 5710–5715 (2008).
37. Peng, A.W., Effertz, T. & Ricci, A.J. Adaptation of mammalian auditory hair cell mechanotransduction is independent of calcium entry. *Neuron* **80**, 960–972 (2013).
38. Chen, X.W., Leto, D., Chiang, S.H., Wang, Q. & Saltiel, A.R. Activation of RalA is required for insulin-stimulated glut4 trafficking to the plasma membrane via the exocyst and the motor protein Myo1c. *Dev. Cell* **13**, 391–404 (2007).
39. Lewis, J.H., Greenberg, M.J., Laakso, J.M., Shuman, H. & Ostap, E.M. Calcium regulation of myosin-I tension sensing. *Biophys. J.* **102**, 2799–2807 (2012).
40. Zhu, T., Sata, M. & Ikebe, M. Functional expression of mammalian myosin Iβ: analysis of its motor activity. *Biochemistry* **35**, 513–522 (1996).
41. Manceva, S. *et al.* Calcium regulation of calmodulin binding to and dissociation from the myo1c regulatory domain. *Biochemistry* **46**, 11718–11726 (2007).
42. Lieto-Trivedi, A. & Coluccio, L.M. Calcium, nucleotide, and actin affect the interaction of mammalian Myo1c with its light chain calmodulin. *Biochemistry* **47**, 10218–10226 (2008).
43. Mazzolini, R. *et al.* Brush border Myosin Ia has tumor suppressor activity in the intestine. *Proc. Natl. Acad. Sci. USA* **109**, 1530–1535 (2012).
44. Tokuo, H. & Coluccio, L.M. Myosin-1c regulates the dynamic stability of E-cadherin-based cell-cell contacts in polarized Madin-Darby canine kidney cells. *Mol. Biol. Cell* **24**, 2820–2833 (2013).
45. Gillespie, P.G. & Cyr, J.L. Calmodulin binding to recombinant myosin-1c and myosin-1c IQ peptides. *BMC Biochem.* **3**, 31 (2002).
46. Whittaker, M. & Milligan, R.A. Conformational changes due to calcium-induced calmodulin dissociation in brush border myosin I-decorated F-actin revealed by cryoelectron microscopy and image analysis. *J. Mol. Biol.* **269**, 548–557 (1997).
47. Greenberg, M.J., Lin, T.M., Goldman, Y.E., Shuman, H. & Ostap, M. Myosin IC generates power over a range of loads via a new tension-sensing mechanism. *Proc. Natl. Acad. Sci. USA* **109**, E2433–E2440 (2012).
48. Laakso, J.M., Lewis, J.H., Shuman, H. & Ostap, E.M. Myosin I can act as a molecular force sensor. *Science* **321**, 133–136 (2008).
49. DeMaria, C.D., Soong, T.W., Alseikhan, B.A., Alvania, R.S. & Yue, D.T. Calmodulin bifurcates the local Ca^{2+} signal that modulates P/Q-type Ca^{2+} channels. *Nature* **411**, 484–489 (2001).
50. Grabarek, Z. Structural basis for diversity of the EF-hand calcium-binding proteins. *J. Mol. Biol.* **359**, 509–525 (2006).

ONLINE METHODS

Constructs and protein expression. The coding sequence of *Myo1c* (NP_001074243.1, residues 698–1028) was PCR amplified from the mouse full length *Myo1c* and cloned into a pET vector together with human CaM (NP_008819.1). The Myo1c–CaM complex was coexpressed in BL21 (DE3) *Escherichia coli* cells. The His_6-tagged proteins were purified with a Ni^{2+}-nitrilotriacetic acid agarose column and subsequent size-exclusion chromatography. All truncation and point mutations of Myo1c used in the current study were created with the standard PCR-based mutagenesis method and conformed by DNA sequencing. For heterologous cell expression, the full-length *Myo1c* (a gift from C. Petit) was cloned into the pRFP vector and is referred to as wild-type RFP-Myo1c. The wild-type GFP–Myo1c IQ3-852 was cloned into the pEGFP-C3 vector.

FPLC coupled with static light scattering. Protein samples (100 µl at a concentration of 20 µM, preequilibrated with corresponding column buffer) was injected into an AKTA FPLC system with a Superose 12 10/300 GL column (GE Healthcare) with the column buffer of 50 mM Tris-HCl, 100 mM NaCl, and 1 mM DTT, pH 7.8. EDTA (1 mM) or $CaCl_2$ (1 mM) was added when necessary. The chromatography system was coupled to a static light-scattering detector (miniDawn, Wyatt) and differential refractive index detector (Optilab, Wyatt). Data were analyzed with ASTRA 6 (Wyatt).

Crystallography. Crystals of Myo1c in complex with apo-CaM (16 mg/ml in 50 mM Tris, pH 7.8, 100 mM NaCl, 5 mM EDTA, and 1 mM DTT) were obtained by hanging-drop vapor-diffusion methods at 16 °C. The crystals were grown in buffer containing 2.0 M ammonium sulfate, 5% 1,4-dioxane, and MES, pH 6.5. To prepare gold derivatives, crystals were soaked in crystallization solution with 2 mM $KAu(CN)_2$ for 2 d. Crystals were soaked in crystallization solution containing 3.0 M ammonium sulfate for cryoprotection. Both native and derivative data sets were collected at the Shanghai Synchrotron Radiation Facility at 100 K. Native data were collected at wavelength at 0.9793 Å, and derivative data were collected at wavelength at 0.9030 Å. Data were processed and scaled with HKL2000 (ref. 51).

Two gold sites were found by SHELXD[52]. The sites' refinement and phase improvement were done by autoSHARP[53]. Three CaMs (PDB 2IX7)[34] and one PH domain (PDB 1W1G)[54] were placed in the density map with MOLREP[55]. The model was further improved by manual rebuilding with COOT[56]. Molecular replacement with the rebuilt model was carried out against the native data set with PHASER[57]. Further manual model building and refinement were completed iteratively with COOT and PHENIX[58]. The final model was validated by MolProbity[59], which indicated residues in the Ramachandran plot with 90.6% in preferred regions, 9.4% in allowed regions and none in disallowed regions. The final refinement statistics are summarized in **Table 1**. All structure figures were prepared with PyMOL (http://www.pymol.org).

Analytical ultracentrifugation. Sedimentation velocity (SV) experiments were carried out on a Beckman XL-I analytical ultracentrifuge equipped with an eight-cell rotor at 25 °C. For SV, the final sedimentation-velocity data were analyzed and fitted to a continuous sedimentation coefficient–distribution model with the fitting results shown as solid lines with Sedfit (http://www.analyticalultracentrifugation.com/default.htm).

Isothermal titration calorimetry assay. Isothermal titration calorimetry (ITC) measurements were carried out on a VP-ITC MicroCal calorimeter (MicroCal) at 25 °C. The titration buffer contained 50 mM Tris-HCl, 100 mM NaCl, 1 mM DTT, pH 7.8, and 1 mM EDTA or 1 mM $CaCl_2$. Each titration point was performed by injection of 10 µL of 200 µM CaM into various peptides in the cell at a time interval of 120 s to ensure that the titration peak returned to the baseline. The titration data were analyzed by Origin7.0 (MicroCal).

NMR spectroscopy. All protein samples for NMR experiments were concentrated to ~0.2 mM in 20 mM Tris buffer containing 100 mM NaCl, 1 mM DTT and 5 mM EDTA (or 5 mM Ca^{2+}) at pH 7.0 in 90% H_2O and 10% D_2O. NMR spectra were acquired at 35 °C on Varian Inova 800 or 750 MHz spectrometers.

Cell culture, immunostaining, image analysis and quantification. COS-7 cells were transiently transfected with 0.5 µg of each plasmid per well with a Lipofectamine PLUS Kit (Invitrogen) in 12-well plates, and cells were cultured for 24 h in DMEM containing 10% FBS in 10% CO_2 before fixation. MDCK cells were transfected with a nucleotransfection kit (Amaxa) by electroporation, and cells were cultured 72 h for polarization in DMEM containing 10% FBS in 10% CO2 before fixation. COS-7 cells were imaged with a TE2000E inverted fluorescent microscope (Nikon), and polarized MDCK cells were imaged with an LSM 710 laser-scanning confocal microscope (Zeiss). Anti–ZO-1 antibody (DSHB, R26.4C, 1:100 dilution) and anti–E-cadherin antibody (DSHB, rr1, 1:50 dilution) were purchased. The validation information and references can be found at the manufacturers' websites. ZEN software (Zeiss) was used to analyze MDCK cell images. Cell lines were maintained under standard conditions, with mycoplasma testing every month.

51. Otwinowski, Z. & Minor, W. Processing of X-ray diffraction data collected in oscillation mode. *Methods Enzymol.* **276**, 307–326 (1997).
52. Sheldrick, G.M. A short history of SHELX. *Acta Crystallogr. A* **64**, 112–122 (2008).
53. Vonrhein, C., Blanc, E., Roversi, P. & Bricogne, G. Automated structure solution with autoSHARP. *Methods Mol. Biol.* **364**, 215–230 (2007).
54. Komander, D. *et al.* Structural insights into the regulation of PDK1 by phosphoinositides and inositol phosphates. *EMBO J.* **23**, 3918–3928 (2004).
55. Vagin, A. & Teplyakov, A. MOLREP: an automated program for molecular replacement. *J. Appl. Crystallogr.* **30**, 1022–1025 (1997).
56. Emsley, P., Lohkamp, B., Scott, W.G. & Cowtan, K. Features and development of Coot. *Acta Crystallogr. D Biol. Crystallogr.* **66**, 486–501 (2010).
57. Mccoy, A.J. *et al.* Phaser crystallographic software. *J. Appl. Crystallogr.* **40**, 658–674 (2007).
58. Adams, P.D. *et al.* PHENIX: a comprehensive Python-based system for macromolecular structure solution. *Acta Crystallogr. D Biol. Crystallogr.* **66**, 213–221 (2010).
59. Chen, V.B. *et al.* MolProbity: all-atom structure validation for macromolecular crystallography. *Acta Crystallogr. D Biol. Crystallogr.* **66**, 12–21 (2010).